

Environments of extended radio sources in the Australia Telescope Low-Brightness Survey

K. Thorat,^{1,2*} L. Saripalli¹ and R. Subrahmanyan^{1,3}

¹Raman Research Institute, C. V. Raman Avenue, Sadashivanagar, Bangalore 560080, India

²Joint Astronomy Programme, Indian Institute of Science, Bangalore 560012, India

³National Radio Astronomy Observatory, Socorro, NM 87801, USA

Accepted 2013 June 26. Received 2013 June 25; in original form 2012 October 2

ABSTRACT

We present a study of the environments of extended radio sources in the Australia Telescope Low-Brightness Survey (ATLBS). The radio sources were selected from the ATLBS Extended Source Sample, which is a well defined sample containing the most extended of radio sources in the ATLBS sky survey regions. The environments were analysed using 4-m Cerro-Tololo Inter-American Observatory Blanco telescope observations carried out for ATLBS fields in the Sloan Digital Sky Survey r' band. We have estimated the properties of the environments using smoothed density maps derived from galaxy catalogues constructed using these optical imaging data. The angular distribution of galaxy density relative to the axes of the radio sources has been quantified by defining anisotropy parameters that are estimated using a new method presented here. Examining the anisotropy parameters for a subsample of extended double radio sources that includes all sources with pronounced asymmetry in lobe extents, we find good evidence for environmental anisotropy being the dominant cause for lobe asymmetry in that higher galaxy density occurs almost always on the side of the shorter lobe, and this validates the usefulness of the method proposed and adopted here. The environmental anisotropy parameters have been used to examine and compare the environments of Fanaroff–Riley Class I (FRI) and Fanaroff–Riley Class II (FR II) radio sources in two redshift regimes ($z < 0.5$ and $z > 0.5$). Wide-angle tail sources and head–tail sources lie in the most overdense environments. The head–tail source environments (for the HT sources in our sample) display dipolar anisotropy in that higher galaxy density appears to lie in the direction of the tails. Excluding the head–tail and wide-angle tail sources, subsamples of FRI and FR II sources from the ATLBS appear to lie in similar moderately overdense environments, with no evidence for redshift evolution in the regimes studied herein.

Key words: methods: data analysis – methods: miscellaneous – galaxies: evolution – galaxies: photometry – radio continuum: general.

1 INTRODUCTION

The Australia Telescope Low-Brightness Survey (ATLBS; Subrahmanyan et al. 2010) is a radio continuum survey at 1.4 GHz of a moderately large region of 8.4 deg^2 of the southern sky. The ATLBS has imaged radio sources with excellent surface brightness sensitivity and hence constitutes a useful resource for studies of structural types. High-resolution radio images of the survey regions are presented in Thorat et al. (2013) along with a discussion of the source counts.

A subset of extended radio sources detected in the survey constitutes the ATLBS Extended Source Sample (ATLBS-ESS; Saripalli

et al. 2012); it contains radio galaxies observed to have the largest angular size and includes all sources with angular size > 30 arcsec. The examination of ATLBS-ESS source structures has yielded subsamples of restarted radio galaxy candidates, $z > 0.5$ low-power radio galaxies, giant radio galaxies and other morphological types. The variety of radio structures detected and their relative abundance has been used to infer the life cycles of radio sources.

Obviously, the gas environments in which radio sources reside and evolve ought to have a substantial influence on the structures that form; this expectation has been vindicated in many case studies where the radio structures have been compared with the X-ray gas environments (Boehringer et al. 1993; Blanton et al. 2011). Numerous studies of the optical environments of radio galaxies have been carried out previously (Longair & Seldner 1979; Yee & Green 1984; Hill & Lilly 1991; Zirbel 1997). The motivation behind these

*E-mail: kshitij@rri.res.in

studies has been to examine differences between different classes of radio sources, the evolution of environments with cosmic epoch as well as the possibility of identifying clusters/groups of galaxies using radio sources as a tracer (Wing & Blanton 2011).

Several studies have found that the environments of Fanaroff–Riley Class I (FRI)/Fanaroff–Riley Class II (FRII) sources are different, and have a redshift dependence. Although FRI sources are found in richer environments, FRII sources at low redshifts are mostly observed to be hosted by field galaxies, whereas at relatively higher redshifts ($z > 0.5$) the FRII environments appear to be richer (Best et al. 2003; Overzier et al. 2008; Hatch et al. 2011). There have been fewer studies that relate the richness of the environments and morphological asymmetries of radio galaxies. Two investigations by Subrahmanyan et al. (2008) and Safouris et al. (2009) are noteworthy in this regard where the radio structures of two giant radio galaxies were examined in the context of the large-scale galaxy distributions in their vicinity (also see Chen et al. 2012 and references therein). The study was also used to infer properties of the ambient thermal gas medium in which the structures evolved. Clear correlations between structural asymmetries and associated extended emission-line gas were also found for radio galaxies that have relatively smaller sizes of a few hundred kpc (McCarthy, van Breugel & Kapahi 1991).

Examining the environments of radio galaxy hosts has been one of the primary aims of the ATLBS. Towards this goal as well as to obtain properties of the host galaxies multiband optical observations were carried out. In this paper we report on the optical observations and use this resource in an attempt to characterize the environments of the ATLBS-ESS radio sources.

The outline of the paper is as follows. In the next section, we describe the sample definition and selection process. In Section 3 we describe the optical observations and data reduction. In Section 4 we describe the photometry. In Section 5 we derive the redshift–magnitude relation that we subsequently use to estimate redshifts for those sources in the sample that lack spectroscopic redshift measurements. Section 6 presents a description of the method adopted to quantify the environmental richness and spatial distribution relative to the radio axes. The last section is a presentation and discussion of the results of the study. We have used a Λ cold dark matter (Λ CDM) cosmology with $H_0 = 71 \text{ km s}^{-1} \text{ Mpc}^{-1}$ and $\Omega_\Lambda = 0.73$.

2 SAMPLE DEFINITION AND SELECTION

We have chosen to restrict our study of the environments of ATLBS sources to those that are extended and hence to a subset of the ATLBS-ESS sources. Briefly, the ATLBS-ESS subsample consists of 119 radio sources that have angular size exceeding 0.5 arcmin. We have omitted sources where no magnitude or redshift information is available. Additionally, since radio galaxies at high redshifts may suffer from greater incompleteness in the detection of neighbouring galaxies, we have imposed a redshift cut, choosing only sources below redshift of $z = 1$. We also reject those sources which are near the edges of the optical images so that the environmental information is not truncated in sky projection: in practice we have rejected sources within a linear distance of 0.5 Mpc of the image edge (for more discussion on this see Section 6.2).

The final sample of sources chosen for the environment study has 43 sources (Fig. 1 presents images of sources of different morphologies from the selected sample). In Table 1 we present this source list. For these most extended of ATLBS radio sources, with good structural information and hence well classified morphology, we

attempt to examine the environments in relation to different source classifications and radio structure.

3 OBSERVATIONS AND DATA REDUCTION

The ATLBS covers two adjacent regions in the southern sky, which we refer to as ATLBS regions A and B. These are centred at RA: $00^{\text{h}}35^{\text{m}}00^{\text{s}}$, Dec.: $-67^{\circ}00'00''$ and RA: $00^{\text{h}}59^{\text{m}}17^{\text{s}}$, Dec.: $-67^{\circ}00'00''$ (J2000 epoch), respectively. The radio observations were carried out using the Australia Telescope Compact Array (ATCA). Details of the radio observations and imaging have been presented in Subrahmanyan et al. (2010) and Thorat et al. (2013).

Follow-up optical observations were carried out with the 4-m Blanco Telescope at Cerro-Tololo Inter-American Observatory (CTIO), Chile. The observations were carried out in Sloan Digital Sky Survey (SDSS) r' , g' and z' bands, using the Mosaic II imager. Each optical image covers $37 \times 37 \text{ arcmin}^2$ area in the sky. The Mosaic II imager covers each image with two rows of eight CCDs, each of them 2048 pixels wide and 4096 pixels long, giving a scale of $0.27 \text{ arcsec pixel}^{-1}$. In this work we have used only the r' -band images.

The observations in r' band were carried out over a complete night and part of the subsequent night. The observations were designed so as to cover each of regions A and B with 14 telescope pointings that tiled the individual regions with some overlap. Each pointing position was observed as five consecutive integrations that were made with the telescope pointing slightly dithered from the nominal pointing position: one integration was with the telescope at the pointing centre and the remaining four were made with about arcmin offsets towards north, south, east and west. The multiple dithered exposures were made to exclude artefacts associated with CCD errors as well as cosmic rays. Each pointing was observed for $5 \times 100 \text{ s}$. The observing night included six exposures towards standard stars; calibration data include bias exposures and flat-fields.

The calibration and construction of images from this data were carried out with the Image Reduction and Analysis Facility (IRAF) software. We have used the ‘MSCRED’ package of IRAF extensively, which has been written for use with Mosaic data. Each image was bias and overscan corrected, corrected for cross-talk, trimmed and flat-fielded in the calibration process. The images have an overscan region of 50 pixels and this was used to correct the entire image for the mean bias. We have in total 20 bias frames that were combined to form a master bias frame, which was used for correction of variable bias in the images. The cross-talk correction was done using the cross-talk correction files provided for the Mosaic II imager by National Optical Astronomy Observatory (NOAO). We have also identified and generated masks that identify erroneous pixels in each of the images. These contain saturated pixels and bleed trails along with pixels known to be faulty in the Mosaic II imager. The saturated pixels were identified with the help of the saturation values recorded in the header. The bleed trails were identified using a minimum trail length of 20 pixels and a pixel value one-third of saturation value. We removed the bleed trails in the images by excluding these pixels and interpolating over them using surrounding pixels. For the purpose of flat-fielding, dome flats were combined to make a master dome flat. For a more accurate flat-fielding, we have constructed a ‘supersky flat’ from observed images. For doing this, we first created object masks for all the target frames, removed the objects from the images using the masks and then combined them into a single image that represents the supersky flat. After flat-fielding using this image the variations in the image response are estimated to be at the 2 per cent level.

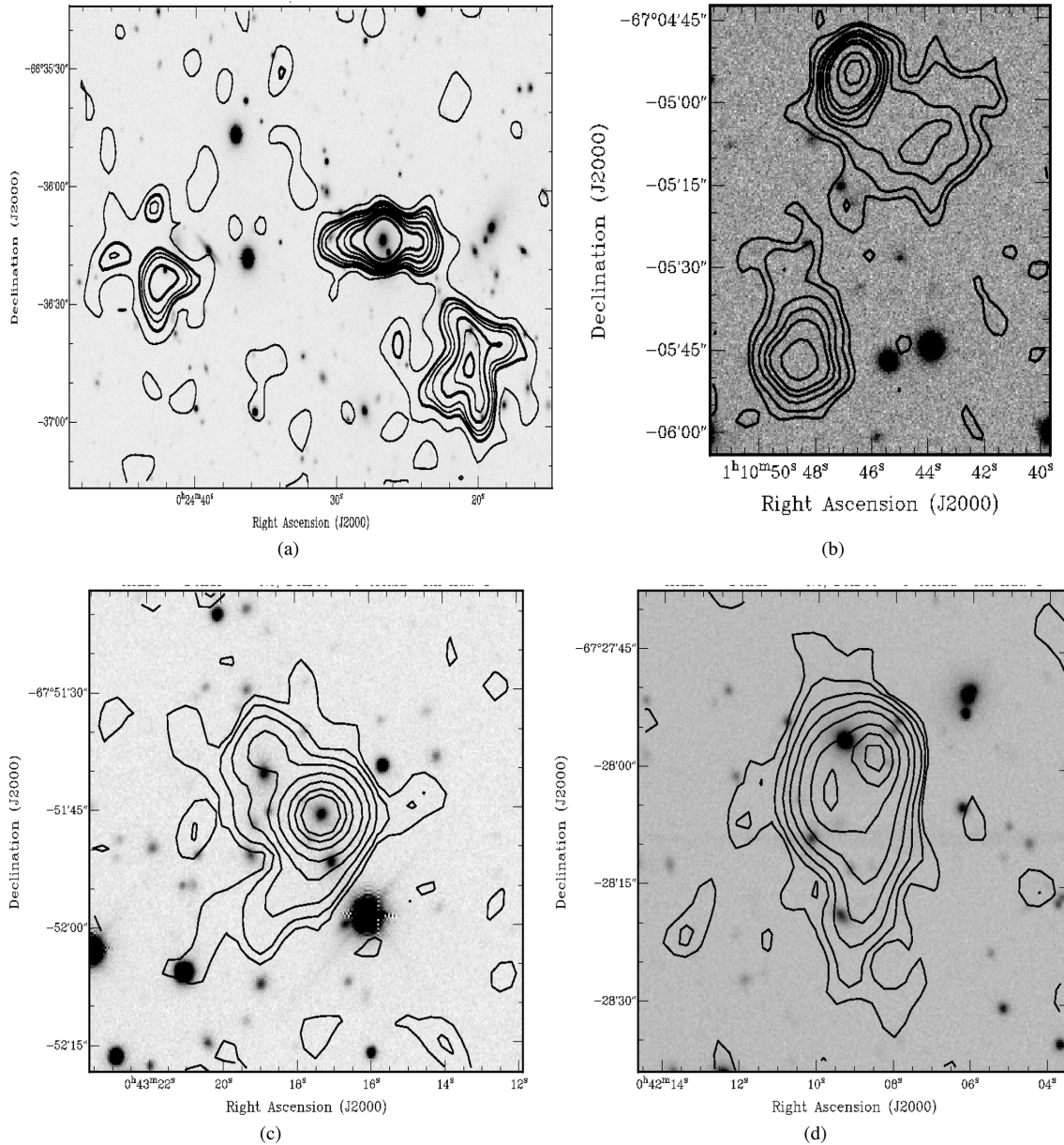


Figure 1. (a) The radio source J0024.4–6636, a FRI source. The source is also an asymmetric source. The radio contours are at $1, 2, 2.5, 3, 4, 5, 6, 8 \times 10^{-4} \text{ Jy beam}^{-1}$. (b) The radio source J0110.7–6705, a FRII source. The radio contours are at $1, 2, 4, 6, 8, 12, 16, 32, 48 \times 10^{-4} \text{ Jy beam}^{-1}$. (c) The radio source J0043.2–6751, a WAT source. The radio contours are at $1, 2, 4, 8, 16, 32, 48, 64 \times 10^{-4} \text{ Jy beam}^{-1}$. (d) The radio source J0042.1–6728, a HT source. The radio contours are at $1, 2, 4, 8, 16, 32, 48, 64 \times 10^{-4} \text{ Jy beam}^{-1}$. The grey-scale in each of the above is optical taken from SDSS r' -band images, described in this paper. The examples of the sources given here show the same sources and follow the same contours as figs 1.5 (right-hand panel), 1.117, 1.48 and 1.47 from Saripalli et al. (2012).

We found that the world coordinate system (WCS) attached to the raw images was inaccurate. An accurate WCS is essential for correct stacking of the dithers and, more importantly, for using the images to examine the environments of the radio sources that are in the ATCA radio images. Therefore, we used United States Naval Observatory (USNO) A2.0 R -band catalogues of objects to reconstruct a correct WCS for the images. Objects common to the USNO catalogue and the images were chosen and their positions were matched to construct the new WCS. The resultant WCS shows an rms difference of 0.3 arcsec compared to positions of USNO catalogue objects.

After correcting the WCS, the images corresponding to the five-position dithers were stacked. First, each of the dithered images was

tangent plane projected using sinc-function interpolation; secondly, the images were rescaled to have the same background brightness. The stacking was carried out using averaging with sigma clipping. The stacking procedure removes spurious objects in the dithers, such as satellite trails and cosmic ray trails, as these may not appear in different dithers at the same pixel. The stacked and co-added images were used for the analyses presented herein.

4 PHOTOMETRY

We have used *IRAF* to carry out the initial photometry using exposures on standard stars and derive the photometric parameters for calibration of the target fields. We observed standard stars from the

Table 1. The sample along with the parameters α_k and the standard deviations in each of the parameters. Column 1 gives the source name, with the extended designation given in column 2 [where ‘***’ denotes a source designation taken from the Sydney University Molonglo Sky Survey (SUMSS); Mauch et al. 2003. Columns 3 and 4 give the redshift of the source and the source type, respectively, with ‘*’ denoting spectroscopically measured values for the redshift. Column 5 gives the PA of the sources in degrees. Columns 6–14 present each overdensity parameter and the normalized standard deviations for each parameter. The column for each of the overdensity parameter gives three values: the best estimate of the value of the parameter itself as well as the values it may have at $\pm 5^\circ$ from the listed PA, giving the uncertainty in the parameter due to the uncertainty in PA. (The angle made by the longer radio lobe with the east–west direction, measured from north to east is designated as the PA of the source. For WAT–HT sources, the bisecting direction instead of the direction of the longer lobe is used to determine the radio axis in this study.)

Source name	Extended source name	Redshift	Source type	PA	α_1	σ_{α_1}	α_2	σ_{α_2}	α_3	σ_{α_3}	α_4	σ_{α_4}	α_5	σ_{α_5}
J0024.4–6636	J002426–663612	0.21	I	90	2.57 ^{+2.57} _{-2.57}	0.4	0.09 ^{+0.1} _{-0.07}	0.1	-0.15 ^{+0.14} _{-0.16}	0.11	0.03 ^{+0.02} _{-0.04}	0.04	0.04 ^{+0.04} _{-0.03}	0.04
J0025.0–6658	J002500–665804**	0.64	WAT	27	1.31 ^{+1.31} _{-1.31}	0.37	-0.14 ^{+0.14} _{-0.14}	0.1	-0.01 ^{+0.02} _{-0.02}	0.11	-0.01 ^{+0.01} _{-0.05}	0.05	-0.01 ^{+0.01} _{-0.01}	0.04
J0026.4–6721	J002628–672148	0.27*	I	-90	0.97 ^{+0.97} _{-0.97}	0.25	0.09 ^{+0.08} _{-0.09}	0.07	0.08 ^{+0.09} _{-0.07}	0.07	0.02 ^{+0.02} _{-0.03}	0.03	0.03 ^{+0.03} _{-0.02}	0.03
J0026.8–6643	J002648–664402**	0.21	I	207	0.93 ^{+0.93} _{-0.93}	0.4	-0.07 ^{+0.07} _{-0.07}	0.1	-0.01 ^{+0.01} _{-0.01}	0.1	-0.05 ^{+0.05} _{-0.04}	0.04	0 ^{+0.01} _{-0.01}	0.04
J0030.7–6714	J003045–671437**	0.97	I	37	1.07 ^{+1.07} _{-1.07}	0.59	0.13 ^{+0.12} _{-0.13}	0.21	0.08 ^{+0.09} _{-0.07}	0.2	-0.06 ^{+0.06} _{-0.11}	0.11	0.01 ^{+0.02} _{-0.02}	0.09
J0031.1–6642	J003108–664245**	0.77	II	-6	0.65 ^{+0.65} _{-0.65}	0.47	-0.07 ^{+0.06} _{-0.07}	0.13	0.06 ^{+0.06} _{-0.07}	0.14	0.02 ^{+0.03} _{-0.05}	0.06	-0.03 ^{+0.03} _{-0.03}	0.06
J0032.9–6614	J003257–661417**	0.92*	I	-34	1.63 ^{+1.63} _{-1.63}	0.58	-0.55 ^{+0.57} _{-0.53}	0.19	0 ^{+0.15} _{-0.25}	0.19	-0.06 ^{+0.05} _{-0.09}	0.09	-0.04 ^{+0.05} _{-0.03}	0.09
J0033.4–6714	J003329–671415**	0.41*	I	239	1.33 ^{+1.33} _{-1.33}	0.25	0 ^{+0.09} _{-0.11}	0.06	0.14 ^{+0.15} _{-0.15}	0.06	0 ^{+0.11} _{-0.05}	0.03	-0.06 ^{+0.04} _{-0.08}	0.03
J0035.0–6612	J003501–661252**	0.47*	I	187	1.61 ^{+1.6} _{-1.6}	0.32	0.12 ^{+0.12} _{-0.12}	0.07	0 ^{+0.01} _{-0.01}	0.07	-0.05 ^{+0.05} _{-0.04}	0.04	0 ^{+0.01} _{-0.01}	0.03
J0036.9–6645	J003654–664513	0.23	I	63	1.21 ^{+1.21} _{-1.21}	0.34	-0.07 ^{+0.06} _{-0.08}	0.1	-0.08 ^{+0.09} _{-0.08}	0.1	0.03 ^{+0.03} _{-0.04}	0.04	-0.04 ^{+0.04} _{-0.05}	0.04
J0040.2–6553	J004014–655325	0.51*	II	243	1.31 ^{+1.3} _{-1.3}	0.3	-0.07 ^{+0.08} _{-0.07}	0.09	0.05 ^{+0.04} _{-0.06}	0.09	0.02 ^{+0.03} _{-0.03}	0.03	-0.02 ^{+0.02} _{-0.03}	0.04
J0041.7–6726	J004145–672629**	0.29*	HT	256	3.32 ^{+3.32} _{-3.32}	0.45	-0.02 ^{+0.03} _{-0.02}	0.09	0.06 ^{+0.06} _{-0.06}	0.09	0.02 ^{+0.02} _{-0.03}	0.03	-0.02 ^{+0.02} _{-0.02}	0.03
J0042.1–6728	J004208–672805**	0.25	HT	180	2.97 ^{+2.97} _{-2.97}	0.48	0.23 ^{+0.22} _{-0.25}	0.09	0.18 ^{+0.2} _{-0.16}	0.11	-0.04 ^{+0.02} _{-0.03}	0.03	-0.14 ^{+0.15} _{-0.13}	0.03
J0043.2–6751	J004317–675147**	0.38	WAT	90	3.01 ^{+3.01} _{-3.01}	0.32	-0.06 ^{+0.08} _{-0.05}	0.09	0.19 ^{+0.18} _{-0.19}	0.08	0.07 ^{+0.07} _{-0.04}	0.04	0 ^{+0.01} _{-0.02}	0.04
J0043.6–6624	J004337–662447	0.99	WAT	124	0.46 ^{+0.46} _{-0.46}	0.74	0.05 ^{+0.05} _{-0.05}	0.25	0 ^{+0.01} _{-0.01}	0.27	0.01 ^{+0.13} _{-0.13}	0.13	0.05 ^{+0.05} _{-0.05}	0.11
J0044.3–6746	J004419–674657**	0.29	II	198	1.73 ^{+1.73} _{-1.73}	0.36	0.19 ^{+0.19} _{-0.2}	0.1	0.04 ^{+0.06} _{-0.02}	0.1	0.02 ^{+0.03} _{-0.04}	0.04	-0.06 ^{+0.05} _{-0.06}	0.04
J0044.7–6656	J004451–665628**	0.72	II	55	2.02 ^{+2.02} _{-2.02}	0.4	-0.19 ^{+0.19} _{-0.19}	0.11	0.05 ^{+0.03} _{-0.06}	0.11	-0.03 ^{+0.03} _{-0.05}	0.05	-0.02 ^{+0.03} _{-0.02}	0.05
J0045.5–6726	J004532–672635**	0.27	I	72	1.93 ^{+1.93} _{-1.93}	0.46	0.01 ^{+0.01} _{-0.05}	0.1	0.21 ^{+0.21} _{-0.21}	0.09	0.01 ^{+0.01} _{-0.05}	0.03	0.13 ^{+0.13} _{-0.13}	0.03
J0046.2–6637	J004613–663708**	0.37	II	135	1.75 ^{+1.75} _{-1.75}	0.36	0 ^{+0.19} _{-0.21}	0.08	0.09 ^{+0.11} _{-0.07}	0.11	0.05 ^{+0.05} _{-0.05}	0.05	-0.01 ⁺⁰ _{-0.02}	0.04
J0049.3–6703	J004922–670358	0.47	I	240	0.68 ^{+0.68} _{-0.68}	0.29	-0.04 ^{+0.04} _{-0.04}	0.08	0 ^{+0.01} _{-0.01}	0.07	-0.01 ⁺⁰ _{-0.03}	0.03	-0.03 ^{+0.03} _{-0.03}	0.03
J0052.7–6651	J005248–665109**	0.24	HT	-45	2.39 ^{+2.39} _{-2.39}	0.44	-0.04 ^{+0.06} _{-0.03}	0.1	0.19 ^{+0.19} _{-0.19}	0.1	0.06 ^{+0.06} _{-0.04}	0.05	-0.01 ⁺⁰ _{-0.03}	0.04
J0055.7–6610	J005548–661031**	0.22	HT	56	1.92 ^{+1.92} _{-1.92}	0.3	-0.06 ^{+0.07} _{-0.05}	0.1	0 ^{+0.1} _{-0.11}	0.08	0.01 ⁺⁰ _{-0.03}	0.03	0.07 ^{+0.07} _{-0.07}	0.04
J0056.4–6651	J005627–665122**	0.19	WAT	-45	2.13 ^{+2.13} _{-2.13}	0.44	0.01 ^{+0.02} _{-0.02}	0.09	-0.11 ^{+0.11} _{-0.12}	0.09	-0.05 ^{+0.05} _{-0.04}	0.04	0.02 ^{+0.01} _{-0.03}	0.04
J0056.6–6743	J005637–674343**	0.93	II	79	1.26 ^{+1.26} _{-1.26}	0.51	0.39 ^{+0.38} _{-0.4}	0.19	0.15 ^{+0.12} _{-0.12}	0.2	0.02 ^{+0.03} _{-0.09}	0.09	-0.07 ^{+0.07} _{-0.07}	0.09
J0056.9–6632	J005657–663239	0.25*	II	53	2.03 ^{+2.03} _{-2.03}	0.41	-0.06 ^{+0.06} _{-0.07}	0.07	-0.04 ^{+0.05} _{-0.03}	0.08	0.02 ^{+0.03} _{-0.03}	0.03	0.05 ^{+0.05} _{-0.04}	0.03
J0057.0–6734	J005704–673413	0.31*	II	-90	1.73 ^{+1.73} _{-1.73}	0.32	-0.15 ^{+0.14} _{-0.17}	0.07	-0.15 ^{+0.16} _{-0.13}	0.08	-0.01 ^{+0.01} _{-0.03}	0.03	-0.01 ^{+0.02} _{-0.01}	0.04
J0057.2–6651	J005707–665059	0.24*	I	112	1.82 ^{+1.82} _{-1.82}	0.41	0 ^{+0.1} _{-0.09}	0.08	-0.03 ^{+0.03} _{-0.02}	0.08	-0.03 ^{+0.04} _{-0.03}	0.03	0.04 ^{+0.04} _{-0.05}	0.03
J0057.4–6703	J005728–670325**	0.26*	WAT	225	3.13 ^{+3.13} _{-3.13}	0.35	-0.05 ^{+0.04} _{-0.06}	0.1	-0.13 ^{+0.14} _{-0.14}	0.08	0.06 ^{+0.06} _{-0.04}	0.04	0.02 ^{+0.03} _{-0.01}	0.04
J0057.7–6655	J005745–665507	0.66	II	120	0.79 ^{+0.79} _{-0.79}	0.33	0.03 ^{+0.04} _{-0.02}	0.09	-0.07 ^{+0.07} _{-0.08}	0.09	0.05 ^{+0.04} _{-0.05}	0.05	0.07 ^{+0.07} _{-0.06}	0.05
J0059.6–6712	J005941–671254**	0.5	I	180	0.81 ^{+0.81} _{-0.81}	0.26	-0.1 ^{+0.09} _{-0.09}	0.08	0 ^{+0.01} _{-0.01}	0.07	0 ^{+0.03} _{-0.03}	0.03	0.02 ^{+0.02} _{-0.02}	0.03
J0101.1–6600	J010107–660018	0.24	II	174	0.81 ^{+0.81} _{-0.81}	0.3	0.02 ^{+0.02} _{-0.02}	0.07	-0.01 ^{+0.01} _{-0.02}	0.08	0.03 ^{+0.02} _{-0.03}	0.03	0.04 ^{+0.04} _{-0.03}	0.03
J0101.5–6742	J010134–674214**	0.59	WAT	-63	1.29 ^{+1.29} _{-1.29}	0.29	-0.1 ^{+0.09} _{-0.12}	0.07	-0.19 ^{+0.2} _{-0.18}	0.08	-0.02 ^{+0.02} _{-0.03}	0.03	-0.01 ^{+0.01} _{-0.01}	0.04
J0102.6–6658	J010238–665813**	0.61	I	40	1.46 ^{+1.46} _{-1.46}	0.4	0.07 ^{+0.09} _{-0.05}	0.11	-0.24 ^{+0.23} _{-0.25}	0.11	-0.02 ^{+0.03} _{-0.05}	0.05	0.04 ^{+0.03} _{-0.04}	0.04

Table 1 – continued

Source name	Extended source name	Redshift	Source type	PA	a_1	σ_{a_1}	a_2	σ_{a_2}	a_3	σ_{a_3}	a_4	σ_{a_4}	a_5	σ_{a_5}
J0102.9–6722	J010256–672220	0.84	WAT	135	$0.56^{0.56}_{0.56}$	0.54	$0.23^{0.22}_{0.23}$	0.15	$0.06^{0.08}_{0.04}$	0.16	$0.04^{0.04}_{0.07}$	0.07	$-0.04^{-0.03}_{-0.04}$	0.08
J0103.1–6632	J010310–663221	0.4*	I	90	$1.2^{1.2}_{1.2}$	0.31	$0.02^{0.02}_{0.02}$	0.07	$-0.01^{-0.01}_{-0.01}$	0.07	$-0.03^{0.03}_{0.03}$	0.03	$0.02^{0.02}_{0.03}$	0.03
J0103.2–6614	J010315–661425	0.33*	II	186	$1.17^{1.17}_{1.17}$	0.28	$0.02^{0.02}_{0.02}$	0.08	$-0.04^{-0.04}_{-0.05}$	0.08	$0^{0.03}_{0.03}$	0.03	$0.01^{0.01}_{0.01}$	0.03
J0103.7–6632	J010344–663227	0.59	II	-90	$1.2^{1.2}_{1.2}$	0.37	$0.04^{0.05}_{0.03}$	0.11	$-0.12^{-0.12}_{-0.12}$	0.1	$0.02^{0.01}_{0.04}$	0.04	$0.04^{0.05}_{0.04}$	0.05
J0103.7–6747	J010345–674746**	0.33*	I	-63	$2.26^{2.26}_{2.26}$	0.44	$-0.08^{-0.08}_{-0.09}$	0.08	$-0.05^{-0.06}_{-0.04}$	0.08	$0.06^{0.06}_{0.03}$	0.03	$-0.01^{0.02}_{-0.02}$	0.03
J0105.0–6608	J010500–660856**	0.85	II	248	$0.32^{0.32}_{0.32}$	0.59	$-0.04^{-0.03}_{-0.05}$	0.22	$-0.09^{-0.09}_{-0.09}$	0.19	$0.02^{0.01}_{0.08}$	0.08	$0.02^{0.02}_{0.02}$	0.09
J0105.7–6609	J010540–660940**	0.98	II	-85	$0.14^{0.14}_{0.14}$	0.94	$-0.02^{-0.02}_{-0.01}$	0.28	$-0.06^{-0.06}_{-0.05}$	0.31	$0.02^{0.01}_{0.12}$	0.12	$0.01^{0.02}_{0.01}$	0.13
J0106.0–6653	J010601–665337	0.26*	I	63	$1.7^{1.7}_{1.7}$	0.29	$0.15^{0.15}_{0.15}$	0.1	$0.02^{0.04}_{0.01}$	0.09	$0.04^{0.06}_{0.03}$	0.03	$-0.1^{-0.09}_{-0.1}$	0.04
J0108.6–6655	J010838–665527**	0.53*	I	27	$1.27^{1.27}_{1.27}$	0.27	$0.08^{0.07}_{0.08}$	0.08	$0.08^{0.09}_{0.08}$	0.09	$0.01^{0.01}_{0.03}$	0.04	0^0	0.04
J0110.7–6705	J011046–670507**	0.8	II	159	$1.03^{1.03}_{1.03}$	0.64	$-0.19^{-0.21}_{-0.17}$	0.22	$0.21^{0.22}_{0.23}$	0.24	$-0.12^{-0.13}_{-0.09}$	0.09	$0.08^{0.06}_{0.1}$	0.1

field of NGC 458 AB¹ (Alvarado et al. 1995); in the r' band three standard star exposures were made during the first night and one standard star exposure during the second night.

The aim of the photometry is to obtain a relation between the measured instrumental magnitudes and true magnitudes. Since we have target images observed at different airmass, we require to derive the calibration relation as a function of airmass. We fit for a linear measurement equation with two free parameters: an additive term and a coefficient that multiplies the airmass. The relation used is $m_s = C_1 A + C_2$, where C_1 and C_2 are the free parameters. We have used 33 standard stars covering a wide range in intensity to fit for the photometric parameters, and used the IRAF task PHOT to derive the instrumental magnitudes and the PHOTCAL package for the fitting.

For deriving the magnitudes from the optical images we used Source Extractor (SEXTRACTOR; Bertin & Arnouts 1996) in conjunction with the initial photometry as explained above. For object detection, we select pixels above 2.5σ , where σ is the standard deviation of the image rms noise. The rms noise is determined from an area of 64 pixels² around the source. In the vicinity of bright sources the background is modelled using the point spread function and the detection threshold is appropriately raised. We find that for our data, the Kron-like apertures of SEXTRACTOR are well suited to estimating the instrumental magnitudes. This measures the flux in apertures of size $2.5 r_{\text{eff}}$, where r_{eff} is the effective radius given by the first moment of intensity distribution. The flux detected in the aperture is background subtracted; for this the background is determined from image pixels in an annulus of width 20 pixels around the objects.

SEXTRACTOR also identifies objects by estimating the stellarity index in the range 0.0–1.0, where a value of 1.0 corresponds to a star-like object and 0.0 is almost certainly a galaxy. This parameter has been widely used in the literature for the purpose of star–galaxy classification: e.g. Varela, D’Onofrio & Fasano (2009) use it for classification of Wide-field Nearby Galaxy-cluster Survey (WINGS) data, preferring to use it with constrains on the stellarity index. In particular, they catalogue objects with stellarity index less than 0.2 as galaxies and objects greater than 0.8 as stars.

We have estimated galaxy counts from the object catalogue created by SEXTRACTOR. Objects with a stellarity index between 0.0 and 0.4 were assumed to be ‘galaxies’. We have chosen 0.4 as a more relaxed upper limit for the stellarity index to be more inclusive and to avoid losing galaxies with higher stellarity indices. This relaxation admittedly increases the risk of including spurious stars; however, they may be expected only to affect the uncertainty in the parameter estimates without causing systematic errors. In Fig. 2 we compare the derived ATLBS galaxy counts with those from the literature. We have compared our galaxy counts with Zhao et al. (2009) as well Yasuda et al. (2001). While Zhao et al. (2009) present observations of the Extended Groth Strip (EGS) field in u , g and R bands (with their R -band differential counts going deeper than ours), Yasuda et al. (2001) present galaxy counts in SDSS u' , g' , r' , i' and z' filters. Our derived counts (complete to 22.75 mag) agree well with the counts presented in both these works.

5 REDSHIFT–MAGNITUDE RELATION

A study of the galaxy environments of ATLBS radio sources requires estimates for their redshifts. Since only a fraction of the host galaxies of the ATLBS radio sources have spectroscopic redshifts,

¹ http://www-star.fnal.gov/Southern_ugriz/Old/www/NGC_458-AB.html

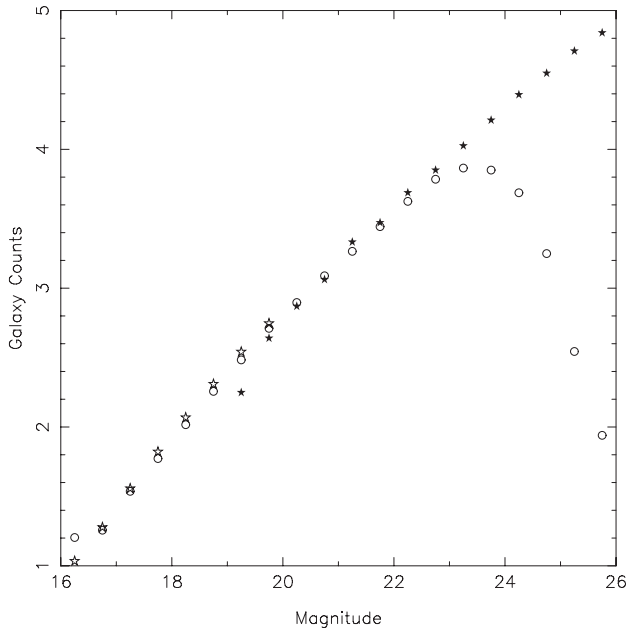


Figure 2. The r' -band galaxy counts for the ATLBS region (displayed using unfilled circles). For comparison with literature, the counts from Zhao et al. (2009) are shown using filled stars and that of Yasuda et al. (2001) are shown using unfilled stars.

we derive here a redshift–magnitude relation for the host galaxies of ATLBS sources, which we use in subsequent sections that explore the galaxy environments.

The ATLBS-ESS sample (Saripalli et al. 2012) was selected based on the angular size of the sources. Of this sample, only 19 radio galaxies have good quality redshift measurements as well as optical magnitudes. To have additional data for deriving a better fit for the relation, we included 61 ATLBS sources that were relatively compact and hence not in the ATLBS-ESS list. These are ATLBS radio galaxies that have good quality redshifts available from our on-going AAOmega observations (Johnston et al., in preparation). We omit quasars while assembling this subsample for deriving the magnitude–redshift relation since their optical magnitudes have contributions from the active galactic nucleus (AGN) at the centre. Most of the subsample of radio galaxies have redshifts in the range 0.2–0.5. We present the sources utilized to derive the redshift–magnitude relation in Table 2.

After producing the r – z plot for these sources, we discovered that 20 of the sources were systematically offset from the principal clustering in the r – z plot. Some of these outliers were spirals or showed spiral-like features; the remainder, though ellipticals, showed clear signs of disturbed optical morphology. Excluding these, we had 80 sources in all to estimate the magnitude–redshift relation.

We fit for coefficients of the equation

$$m_r = a \log_{10} z + b. \quad (1)$$

The fit yielded parameter values $a = 5.752$ and $b = 21.82$, with an rms error of 0.09. These may be compared with corresponding values of $a = 5.3$ and $b = 21.05$ derived by Eales et al. (1997) for R band, and $a = 5.917$ and $b = 21.65$ derived by Gendre, Best & Wall (2010) from the r' -band data of the CONFIG survey. We plot the fitted relation in Fig. 3 along with the data.

6 QUANTIFYING THE GALAXY ENVIRONMENTS OF EXTENDED RADIO SOURCES

While there are many methods in the literature for measuring the environmental richness of extragalactic sources (see Gal 2008, for a review), most rely on the availability of redshifts. When working with a photometric catalogue however, where redshifts are not available for most galaxies, there are fewer methods available for estimating the environmental richness. One of the more common methods used with photometric catalogues is the counts-in-a-cell method, which was used by Abell (1958) to estimate richness of clusters. In this method the overdensity of galaxy counts relative to a mean background density of galaxies is estimated. In determining the environments of radio galaxies, Hill & Lilly (1991), for example, used a variant of this method. However, the latter method has the disadvantage that the galaxies counted in a chosen volume (e.g. near a radio source) would include contamination from galaxies along the line of sight. Additionally, the selected volume may not sample the cluster fully, either in spatial or luminosity (i.e. magnitude) range. The above method gives good estimates of the environmental richness in cases where clusters are a priori known to exist; however, for the purpose of the blind study we are attempting in the work presented herein, which involves estimating environmental richness for regions with no a priori information available, it may not be useful. Another method that has been used for estimation of environmental richness is that using the galaxy–galaxy two-point correlation function (Hardcastle 2004), which has been used to detect galaxy clustering around any specified point of interest. The two-point correlation method has the advantage of not being dependent on a particular form for the structure (e.g. galaxy cluster).

In the work presented here, we adopt the method of spatial filtering as put forward by Postman et al. (1996, hereafter P96). This method gives the large-scale environment of the source under examination in the form of a map as opposed to quantifying the environmental richness at specific points (e.g. host galaxy location). This enables us to characterize environmental anisotropy on the sky relative to the projected geometry of the source.

6.1 Description of the method

The spatial filter method, which has been devised for use when only photometric information is available, is as follows. A smoothed galaxy map is created by using a convolving function, which is a composite of two filters: a spatial filter and a magnitude filter. The filters are chosen so as to match the density profile of a galaxy cluster and the luminosity function.

The spatial filter is the projected cluster radial profile. The form of the radial filter is given by equation (19) from P96:

$$P(r/r_c) = \frac{1}{\sqrt{1 + (r/r_c)^2}} - \frac{1}{\sqrt{1 + (r_{co}/r_c)^2}} \quad \text{for } r < r_{co}$$

$$= 0 \quad \text{otherwise,} \quad (2)$$

where r_c is the cluster core radius and r_{co} is the cut-off radius. In literature, a choice of $1 h^{-1}$ Mpc for the cluster cut-off radius has been made, and the core radius has been adopted to be a factor of 10 smaller at $100 h^{-1}$ kpc (P96 and references therein; Kim et al. 2002). The cut-off radius determines the efficiency in the detection of clusters, more than the actual form of the radial filter (Kim et al. 2002). The smoothing is essentially a spatial filter that rejects structures with scale size well below the cut-off radius; therefore,

Table 2. Sources used to fit the magnitude–redshift relation. Columns 1 and 2 give the RA and Dec. (J2000) of each source, columns 3 and 4 give the same for the optical ID for each radio source. Columns 5 and 6 give the redshift and magnitude for each source.

RA (J2000)	Dec. (J2000)	RA (Id) (J2000)	Dec. (Id) (J2000)	Redshift	m_r
0:22:45.10	−66:53:06.3	0:22:45.10	−66:53:06.3	0.234	18.48
0:26:14.33	−66:45:55.1	0:26:14.41	−66:45:54.9	0.426	20.25
0:26:21.47	−67:13:41.6	0:26:21.54	−67:13:41.7	0.249	18.45
0:26:21.47	−67:13:41.6	0:26:21.54	−67:13:41.7	0.249	18.45
0:26:28.92	−67:21:49.6	0:26:28.52	−67:21:48.8	0.274	18.15
0:26:49.08	−66:31:22.0	0:26:49.10	−66:31:23.0	0.323	19.3
0:26:49.18	−66:44:00.8	0:26:49.09	−66:44:01.1	0.219	17.96
0:27:15.59	−66:24:18.5	0:27:15.59	−66:24:18.1	0.073	15.06
0:27:15.60	−66:24:18.7	0:27:15.50	−66:24:18.6	0.074	15.06
0:27:46.63	−67:49:51.9	0:27:46.64	−67:49:52.5	0.174	16.52
0:27:56.29	−67:37:53.8	0:27:56.28	−67:37:53.8	0.252	17.7
0:28:08.51	−66:14:15.9	0:28:08.55	−66:14:16.5	0.272	19.22
0:28:09.84	−66:29:38.8	0:28:09.73	−66:29:39.0	0.339	18.37
0:28:22.42	−66:53:44.1	0:28:22.41	−66:53:43.5	0.190	17.32
0:28:29.45	−67:18:43.6	0:28:29.47	−67:18:44.3	0.243	17.61
0:28:33.98	−67:21:50.2	0:28:33.98	−67:21:50.3	0.241	17.83
0:28:41.04	−66:43:45.1	0:28:41.19	−66:43:44.5	0.234	18.62
0:28:51.94	−67:58:39.3	0:28:52.02	−67:58:39.9	0.352	18.05
0:29:02.47	−66:39:51.6	0:29:02.65	−66:39:51.9	0.219	18.57
0:29:04.64	−66:03:20.4	0:29:04.58	−66:03:21.4	0.400	19.69
0:29:07.17	−67:22:56.4	0:29:07.12	−67:22:55.6	0.220	17.76
0:29:25.65	−67:21:30.7	0:29:25.55	−67:21:31.5	0.292	19.38
0:29:44.03	−66:56:23.4	0:29:43.95	−66:56:23.3	0.402	19.09
0:29:52.63	−66:06:53.2	0:29:52.98	−66:06:53.5	0.402	21.18
0:30:01.70	−67:14:02.2	0:30:01.69	−67:14:03.3	0.413	18.63
0:30:09.02	−67:26:44.9	0:30:09.18	−67:26:45.1	0.713	21.54
0:30:44.21	−67:36:10.6	0:30:44.32	−67:36:11.1	0.321	19.5
0:31:14.79	−67:18:02.0	0:31:14.68	−67:18:01.5	0.501	20.64
0:31:17.26	−67:50:52.3	0:31:17.12	−67:50:53.2	0.375	19.86
0:31:29.22	−66:55:16.9	0:31:29.37	−66:55:16.8	0.532	20.36
0:31:32.05	−67:48:58.7	0:31:32.49	−67:49:01.1	0.355	19.1
0:31:32.48	−67:49:00.4	0:31:32.50	−67:49:00.5	0.356	19.1
0:31:47.04	−66:20:50.6	0:31:47.05	−66:20:50.4	0.278	19.09
0:31:55.80	−66:44:05.8	0:31:55.81	−66:44:05.1	0.653	20.95
0:32:01.00	−66:44:06.7	0:32:00.86	−66:44:06.4	0.611	20.76
0:32:45.72	−66:29:12.1	0:32:45.69	−66:29:11.9	0.214	18.04
0:33:29.46	−67:14:20.2	0:33:29.35	−67:14:19.2	0.407	18.38
0:33:46.81	−67:38:03.3	0:33:46.69	−67:38:04.7	0.356	18.73
0:33:47.32	−68:00:50.4	0:33:47.48	−68:00:49.8	0.225	18.68
0:33:56.56	−66:52:05.7	0:33:56.48	−66:52:05.4	0.402	19.1
0:34:05.59	−66:39:34.5	0:34:05.59	−66:39:34.5	0.110	16.79
0:34:08.85	−66:26:21.7	0:34:08.98	−66:26:21.7	0.486	19.53
0:34:29.18	−66:45:35.7	0:34:29.19	−66:45:35.6	0.403	19.61
0:34:33.18	−67:36:26.8	0:34:33.12	−67:36:28.4	0.069	14.9
0:34:57.51	−66:30:29.8	0:34:57.44	−66:30:29.6	0.487	20.27
0:35:02.08	−66:12:52.2	0:35:01.97	−66:12:52.5	0.465	19.1
0:35:05.24	−67:41:14.4	0:35:05.08	−67:41:14.5	0.072	15.32
0:35:34.52	−66:07:24.4	0:35:34.55	−66:07:25.6	0.264	19.65
0:35:35.41	−66:56:20.7	0:35:35.33	−66:56:20.0	0.296	19.65
0:35:35.85	−66:18:44.3	0:35:35.80	−66:18:44.3	0.508	20.41
0:36:58.16	−66:34:16.3	0:36:58.17	−66:34:16.4	0.241	18.46
0:36:58.16	−66:34:16.3	0:36:58.17	−66:34:16.4	0.241	18.46
0:37:29.07	−67:02:50.8	0:37:29.06	−67:02:50.3	0.350	18.98
0:39:01.31	−67:49:43.7	0:39:01.39	−67:49:43.5	0.073	15.08
0:39:03.72	−66:54:36.6	0:39:03.69	−66:54:34.7	0.256	18.66
0:40:44.35	−67:24:32.4	0:40:46.67	−67:24:35.8	0.296	19.07
0:40:55.50	−66:50:16.1	0:40:55.46	−66:50:16.5	0.747	20.86
0:41:00.98	−67:24:32.3	0:41:01.05	−67:24:33.0	0.299	18.42
0:41:12.20	−67:51:22.2	0:41:12.33	−67:51:22.1	0.359	20.2
0:41:20.87	−67:08:06.8	0:41:20.92	−67:08:05.2	0.492	20.05
0:41:46.39	−67:26:27.5	0:41:47.29	−67:26:26.8	0.293	17.34
0:41:46.80	−67:26:15.4	0:41:46.80	−67:26:15.4	0.293	19.24

Table 2 – continued

RA (J2000)	Dec. (J2000)	RA (Id) (J2000)	Dec. (Id) (J2000)	Redshift	m_r
0:41:58.21	−66:54:11.6	0:41:58.46	−66:54:11.0	0.520	19.83
0:42:01.69	−67:29:00.8	0:42:01.83	−67:29:03.0	0.296	18.87
0:42:14.21	−66:54:49.4	0:42:14.25	−66:54:48.6	0.161	18.63
0:42:23.49	−66:25:27.9	0:42:23.51	−66:25:28.1	0.210	17.7
0:43:08.54	−66:35:33.2	0:43:08.59	−66:35:33.9	0.318	19.23
0:52:06.50	−66:22:51.9	0:52:07.18	−66:22:55.8	0.704	21.89
0:56:57.22	−66:32:38.8	0:56:57.22	−66:32:38.8	0.249	18.6
0:57:04.57	−67:34:11.8	0:57:04.41	−67:34:12.8	0.307	19.02
0:57:07.00	−66:32:41.4	0:57:07.00	−66:32:41.4	0.248	18.81
0:57:12.34	−66:51:17.5	0:57:06.98	−66:50:59.0	0.236	18.2
0:57:27.20	−67:03:20.9	0:57:27.23	−67:03:18.9	0.260	18.64
0:57:43.62	−67:01:36.2	0:57:43.62	−67:01:36.2	0.261	18.13
0:57:48.60	−67:02:25.1	0:57:48.60	−67:02:25.1	0.064	14.72
1:02:41.48	−67:34:03.1	1:02:41.48	−67:34:03.1	0.065	15.53
1:03:10.45	−66:32:21.2	1:03:09.93	−66:32:21.1	0.398	18.87
1:03:14.16	−66:14:40.0	1:03:14.97	−66:14:24.9	0.331	18.22
1:03:44.44	−67:47:52.4	1:03:44.58	−67:47:52.0	0.329	18.44
1:06:01.66	−66:53:37.0	1:06:01.85	−66:53:37.1	0.262	17.6

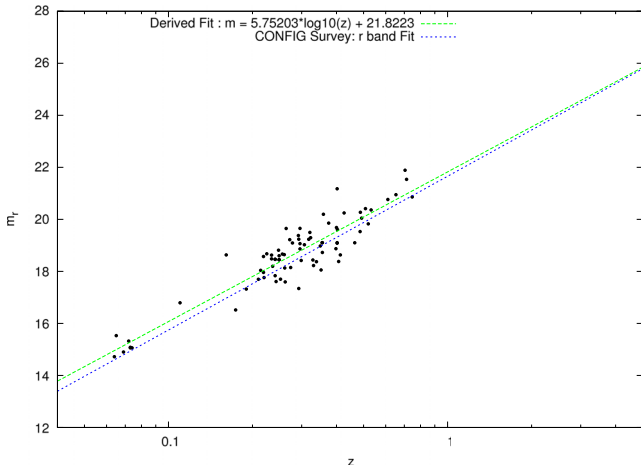


Figure 3. The fitted magnitude–redshift relation is shown as lines along with the data points used in deriving the fits; the data points correspond to the compilation of ATLBS radio galaxies with redshift measurements. The average error in z from this relation is 0.09. For comparison, the relation derived by Gendreau et al. (2010) (CONFIG survey) is also shown.

we have used a somewhat smaller cut-off radius of 0.5 Mpc so that we retain galaxy distribution structures corresponding to relatively poorer clusters. Following P96, we have used a core radius that is a factor of 10 smaller than the cut-off radius: we use $r_c = 50$ kpc.

The magnitude filter has been chosen to be a Schechter luminosity function with the following form:

$$\phi \propto 0.4 \ln(10) 10^{-0.4(m-m_c)(\alpha+1)} e^{-10^{-0.4(m-m_c)}}. \quad (3)$$

We have adopted $\alpha = -1.03$ and m_c , the characteristic magnitude of the luminosity function, to be -20.6 (in absolute magnitude units); these are values typical for galaxy clusters (Popesso et al. 2005).

The matched filtering essentially creates a smoothed image optimized for the detection of clusters whose properties match the filter characteristics. Galaxy clustering structure with properties that deviate from the chosen model would be represented in the smoothed image with reduced prominence. The smoothed image represents the likelihood that a cluster is present at each pixel location and at the redshift of the host galaxy.

We may point to a few drawbacks of the method. The form of the smoothing filter is assumed a priori. This means that any overdensities in the environments that have a form that deviates substantially from the filter, such as a filamentary structure, will be represented with smaller significance. An accurate estimate of the galaxy background (a detailed description of the background is in Section 6.2) is required as a correction to the counts; the background may contain galaxies from both cluster as well as non-cluster galaxies and non-uniformity in the distribution may result in errors in the estimate of the background. This does not cause problems provided the optical images are large and clusters occupy small sky area; however, in smaller images where clusters may be dominant over non-cluster or field galaxies, the erroneous estimate of the background may give incorrect results for the inferred structure at the redshift of interest. The optical r' -band images used herein have a fairly large size (37×37 arcmin²), which obviates the latter concern.

An issue that merits mention is that we have not taken into account the redshift dependence of the core and cut-off radius, or the absolute characteristic magnitude of the cluster or their radial profiles; the clusters at high redshifts may have substantially different parameters than those we have used.

6.2 Implementation of the method

In this section we follow the nomenclature used by P96. We evaluate the output smoothed image with a sampling that is sparse relative to the input image; the output image is evaluated at its ‘pixels’ as a weighted summation over the input image:

$$S(i, j) = \sum_{k=1}^{N_{\text{gal}}} P[r_k(i, j)] L(m_k), \quad (4)$$

where $L(m_k)$ corresponds to

$$L(m) = \frac{\phi(m - m_c)}{b(m)} = \frac{\phi(m - m_c) 10^{-0.4(m - m_c)}}{b(m)}. \quad (5)$$

In the above equation, $b(m)$ is the ‘background’ surface density of galaxies and the factor $10^{-0.4(m - m_c)}$ has been introduced to keep $L(m)$ integrable (see P96). The sum is evaluated at pixels of the output image denoted by the indices (i, j) and the index k is over

all the galaxies in the field (N_{gal} is the total number of galaxies in the field). r_k is the distance from the position of the output pixel to the position of the galaxy with index k , which has an apparent magnitude ‘ m_k ’.

The various terms in the sum $S(i, j)$ are calculated as follows. For a given radio source, for which the environmental richness is to be quantified, a unique smoothed map is created that depends on the source redshift. The characteristic apparent magnitude, the characteristic radius and the cut-off radius for the image corresponding to any radio source depend on its redshift. The characteristic apparent magnitude is determined from the characteristic absolute magnitude using the relation: $M_c = m_c - DM - K$, where DM is the distance modulus and K is the k -correction appropriate to the redshift of the source. The k -correction for our sources below redshift of 0.7 used the analytical expressions of Chilingarian, Melchior & Zolotukhin (2010) for SDSS r' band. We have used the luminous red galaxy (LRG) template results for our galaxies, which gives k -correction as a function only of redshift, and yields results similar to that derived by Fukugita, Shimasaku & Ichikawa (1995) for elliptical galaxies. Beyond redshift 0.7 we have used the k -correction given by Metcalfe et al. (1991) and using galaxy colours given by Fukugita et al. (1995). The distribution function $b(m)$, which is supposed to be the ‘background’ galaxy counts, is taken to be simply the number counts for galaxies in the field that are fainter than magnitude m . This is because we do not know a priori which galaxies belong to the background as opposed to clusters.

The normalization for the sum is determined using the following equations (equations 20 and 21 of P96):

$$\int_0^{\infty} P(r/r_c) 2\pi r dr = 1 \quad (6)$$

and

$$\int_0^{m_{\text{lim}}} \phi(m - m_c) 10^{-0.4(m - m_c)} dm = 1. \quad (7)$$

Here the radial integration is truncated at the cut-off radius due to the form of $P(r)$. The integration over magnitudes is limited by the limiting magnitude m_{lim} of the survey. The normalizations of the radial and magnitude filter produce a background level of unity in the smoothed map (see P96). Therefore, on normalizing, the pixels are expected to have a centrally concentrated distribution about unity, with values exceeding unity representing overdensities. We obtain pixel distributions covering a large range, with a tail towards positive values. The mode of the distribution is close to unity, and depends on the specific galaxy distribution in the image.

We initially made a catalogue of galaxies (objects that have stellarity index less than 0.4) from the optical image, excepting those sources within 200 image pixels from the edge to avoid these regions of higher image noise. Smoothed images with grid size between half the core radius to twice the core radius yield similar results (see P96); therefore, we choose to compute the summation above on a grid of pixels spaced by a distance corresponding to the core radius.

6.3 Parameters quantifying radio source environment

To examine the environments of the radio sources, we have constructed parameters which quantify the environmental overdensity and its distribution in the vicinity of the radio source. For each source, we define a radio axis vector whose direction is taken to be the direction of the longer radio lobe. The angle made by the longer radio lobe with the east–west direction, measured from north

to east is designated as the position angle (PA) of the source. For wide-angle tailed (WAT) and head–tail (HT) sources, the bisecting direction instead of the direction of the larger lobe is used to determine the radio axis in this study. With the radio axis as reference, the smoothed map is resampled.

A circle of 0.5 Mpc radius is constructed centred at the host galaxy of the radio source, and this circular region is further divided into annular rings 100 kpc wide. Along the circumference of each annular region 16 new equidistant grid-pixels are generated at constant angular distance from each other and at constant distance from the host galaxy. The smoothed image values at the new grid-pixels are calculated by interpolating using neighbouring pixels from the original smoothed map. For the annular region defined by each ring five quantities are calculated:

$$a_k = \frac{\sum S_i f_k}{\bar{a}_1}, \quad (8)$$

where the summation is over index ‘ i ’; i.e. over the new grid pixels in the annular region. The functions f_k that weight the values of the pixels are 1, $\sin(\theta_i)$, $\cos(\theta_i)$, $\sin(2\theta_i)$, $\cos(2\theta_i)$ for, respectively, $k = 1, 2, 3, 4$ and 5. The argument of the functions is given by $\theta_i = \theta_{ia} + \pi/2$, where the angle θ_{ia} is the angle of the i th grid-pixel as measured from the radio axis defined above and S_i is the value at the grid pixel. The first quantity simply gives a measure of overdensity in the environment of the radio source. The other four quantities provide information regarding the dipole and quadrupole anisotropy in the environment of the source. All the quantities are normalized by the average of the a_1 estimated for the different annuli for each source.

The ‘ a ’ parameters represent Fourier components of the angular distribution of galaxy overdensity, or more specifically, the amplitudes of a Fourier harmonic decomposition of angular distributions in galaxies about the radio axis. A schematic depiction of the parameters a_2 – a_5 is given in Fig. 4.

The a_1 parameter is the mean overdensity and is the amplitude of the zeroth Fourier component. The a_2 and a_3 parameters are the fractional side-to-side asymmetry in the galaxy distribution; if the angular distribution follows a dipolar asymmetry then this quantity is unity and the two coefficients a_2 and a_3 as well as their signs give the direction of the dipole in the 2D sky plane. The a_4 and a_5 parameters are the quadrupolar anisotropy and are the Fourier components of the next order terms.

The errors in these parameters for any source are calculated by sampling different regions of the smoothed map containing the source and constructing the parameters a_k in those randomly offset regions. This procedure is repeated at 100 random positions offset from each source. As shown above, the quantities a_k are weighted sums of the pixel values in the vicinity of each source. Therefore, we choose to normalize each quantity by the mean of the first parameter a_1 , which represents the average overdensity in the smoothed map. The standard deviations of the five parameters obtained by the above process are also normalized by this \bar{a}_1 . The parameters a_k and their standard deviations for all the sample sources are listed in Table 1.

7 RESULTS AND DISCUSSION

The sources in our sample are divided morphologically into multiple classes. The main classification scheme adopted is the Fanaroff–Riley classification (Fanaroff & Riley 1974). WAT and HT sources are in separate classes. For a discussion of the classification of the sample sources, see Saripalli et al. (2012). Below we describe the results for each of the classes.

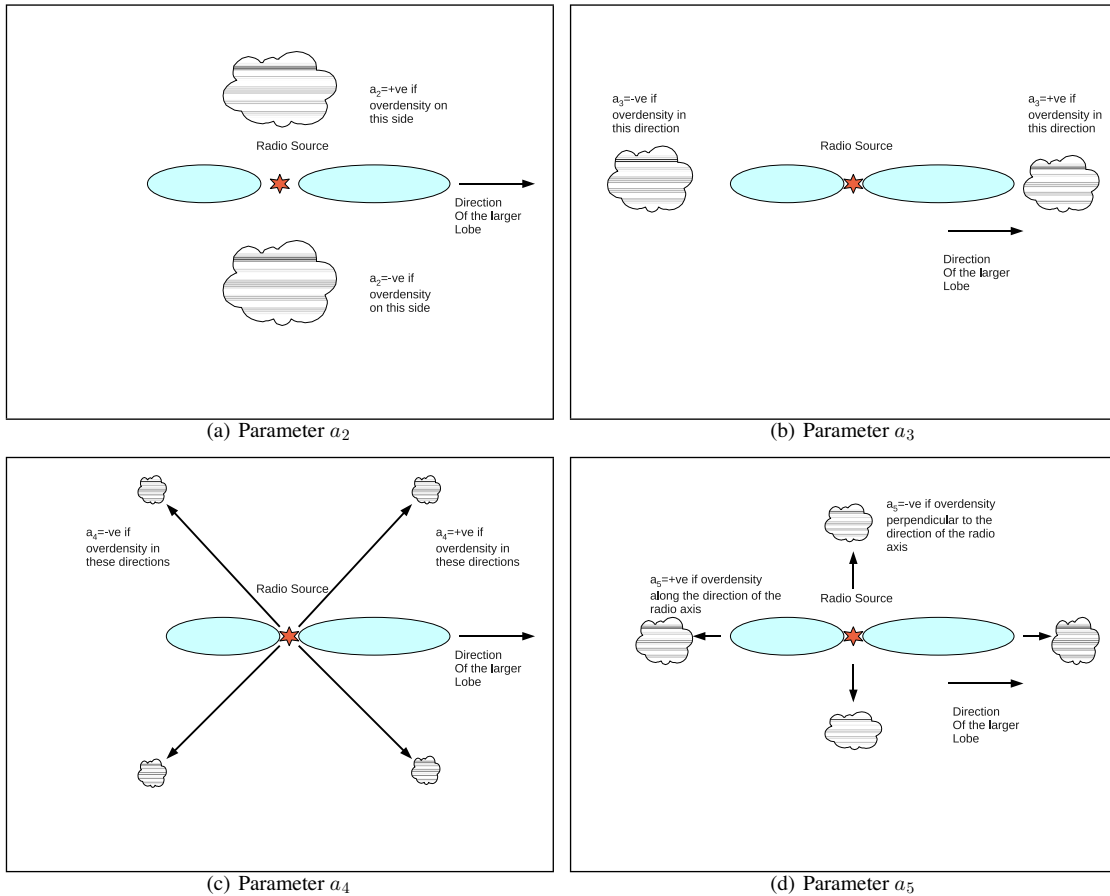


Figure 4. Schematic depiction of the overdensity parameters a_2 – a_5 (panels a–d).

The errors in the derived a_k parameters for the individual sources are indeed substantial (see Table 1). Therefore, while estimating the environment for samples of sources of a particular class, we have improved the confidence by computing a weighted mean of each parameter over the sources in the class: this is equivalent to a stacking of images with a weighting corresponding to the noise in the individual images. We also compute the errors in the weighted means.

7.1 The environments of head–tail and wide-angle tailed ATLBS-ESS sources

Wide-angle tailed and head–tail sources are radio galaxies that show extensive signs of ‘disturbed’ radio morphology. These sources have bent radio jets/lobes. It has been a long held view that the WAT/HT morphology is a result of the interaction of the radio source with cluster gas, either because of ram pressure forces during the movement of the host galaxy through the cluster gas (Owen & Rudnick 1976) or owing to intracluster gas weather created in cluster mergers (Burns et al. 2002). The association of these sources with cluster environments has been taken advantage of to detect galaxy clusters at high redshifts (Best et al. 2003). We expect, therefore, that the WAT/HT sources show evidence of inhabiting rich environments.

In our sample, there are 11 WAT/HT sources. Of the 11 sources, six appear to lie in relatively rich environments (showing values above 2.0 for the parameter a_1 , which gives a measure of the ‘average’ overdensity in the environment of the source). All the

four HT sources in our sample are at relatively low redshifts (below redshift of 0.3) and all four are found in rich environments with weighted mean of $2.465(\pm 0.197)$ for the a_1 parameter. The seven WAT sources also have a high overdensity, with a weighted mean value of $1.969(\pm 0.145)$ for a_1 indicating overdense environments as expected for this class of sources. There is a hint of decreasing overdensity with redshift suggesting that the WATs do not appear to be constrained to overdense regions at higher redshifts. However given the difficulties in detecting faint galaxies at higher redshifts completeness in galaxy counts will certainly be affected at faint galaxy magnitudes ($m_r > 22.75$) and this limits the confidence in the finding of any trend with redshift. Nevertheless, the finding that WAT and HT sources do indeed inhabit relatively rich environments is consistent with previous findings and lends confidence in the new method proposed herein for studies of environments of radio sources. A histogram of the values of a_1 parameter for WAT/HT subsample is presented in Fig. 5(a).

7.2 The environments of FRI and FRII ATLBS-ESS sources

FRI sources have been known to inhabit rich environments: this property has been established with greater confidence for FRIs at relatively lower redshifts. In contrast, FRII sources have been known to favour sparse environments at low redshifts, and are known to reside in richer environments at higher ($z > 0.5$) redshifts (Hill & Lilly 1991; Zirbel 1997). Thus FRII radio sources present a remarkable change in their environments with cosmic epoch. Below

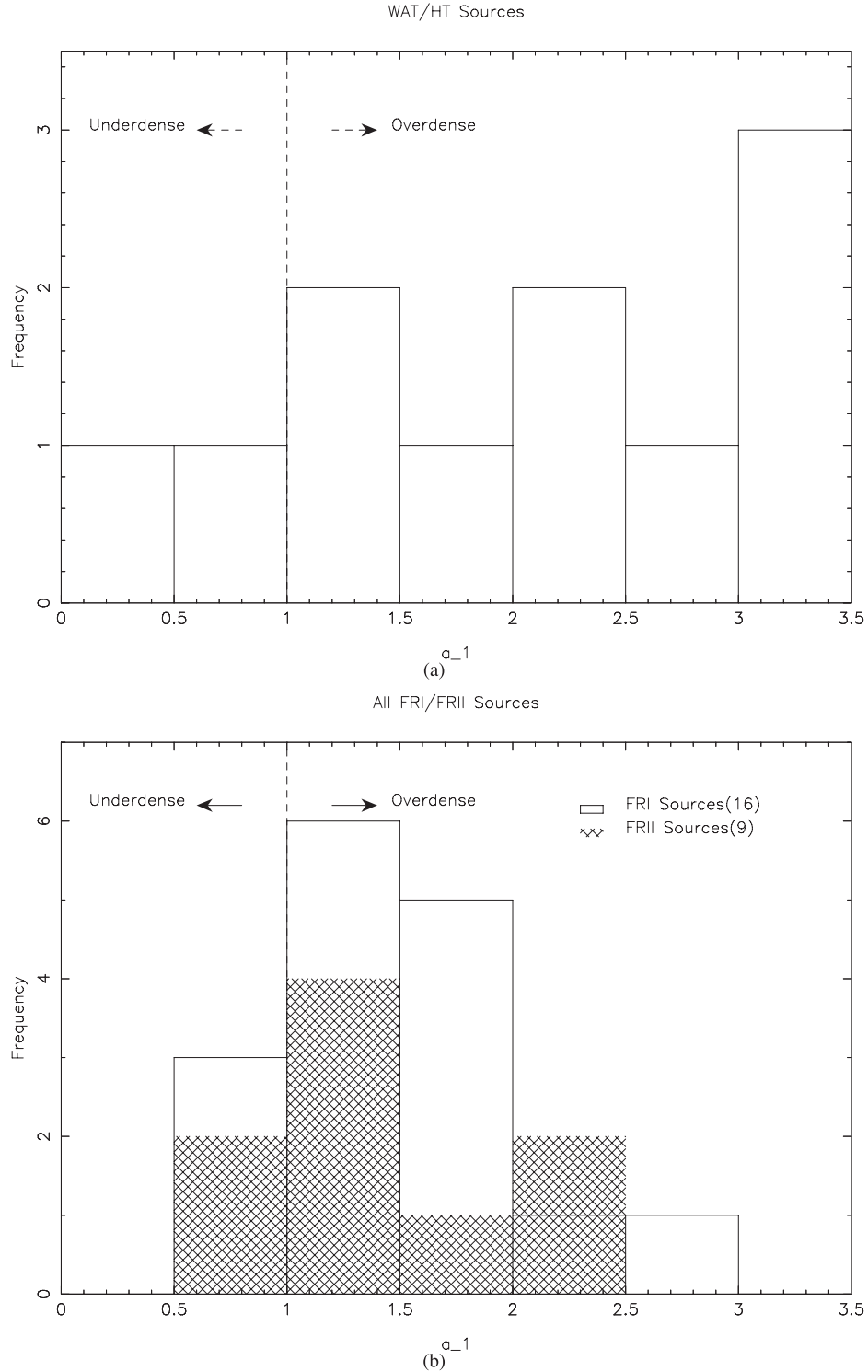


Figure 5. Histograms of a_1 parameter for (a) WAT/HT and (b) FRI/FRII sources.

we discuss the findings from our work for these two classes of sources in our sample.

There are 17 FRI and 15 FRII sources in our sample. The weighted mean value of a_1 for the 17 FRIs is $1.326(\pm 0.08)$ where as the corresponding value for the 15 FRIIs is 1.294 ± 0.098 . The sample includes four FRI sources that have a_1 below 1. These sources are J0026.8–6643, J0026.4–6721, J0049.3–6703 and J0059.6–6712. These sources are not at particularly high redshifts (all of them

have redshifts less than 0.5). However, in the case of the latter two sources, it is possible that imaging artefacts and the presence of bright stars in the vicinity may have played a role in underestimating the environmental overdensity.

We have separated our subsamples of FRI and FRII sources into two redshift regimes, one below redshift 0.5 and another above and we compare their environments in each of these regimes. Environments of FRI sources at high redshifts have remained unexplored

because of sensitivity issues: FRI sources are lower in luminosity and have more diffuse structures making their detection more difficult at high redshifts. ATLBS is a survey with high surface brightness sensitivity and has imaged sky regions with good resolution; the ATLBS has detected several FRI sources with $z > 0.5$ (Saripalli et al. 2012). In our sample of 17 FRIs the redshifts range from 0.21 to 0.97 and there are four at redshifts above 0.5. We may, therefore, attempt an examination of the environments of these FRI sources at relatively high redshifts.

However before we examine the results we remind ourselves that because of the finite limit to the sensitivity neighbouring galaxy counts at higher redshifts will be progressively underestimated. We accordingly interpret our results, and emphasize that the environments of high redshift sources may only be a lower limit.

We find that at redshifts above 0.5, FRI and FRII sources inhabit environments that are not too dissimilar in richness. Moreover, both FRI and FRII type sources are found to lie in relatively overdense environments in the $z > 0.5$ regime. There are nine FRII sources and five FRI sources with $z > 0.5$. However, we have not considered the FRI source J0059.6–6712 in this comparison as it is on the redshift boundary. Two FRII sources J0105.7–6609 and J0057.7–6655 for which the results may have been affected by nearby bright stars, as well the FRII source J0105.0–6608 for which the host galaxy identification is unclear and the source J0056.6–6743 which displays hybrid morphology have been excluded from the exercise. This gives five FRII sources and four FRI sources for the exercise. The average richness (as quantified by the parameter a_1) for $z > 0.5$ FRI sources is 1.335 ± 0.196 as compared to an average value of 1.305 ± 0.177 for the FRII sources at high redshift. Since we are comparing both groups in the same redshift regime, underestimation of galaxy counts will affect both similarly.

FRI sources at low redshifts appear to inhabit a variety of environments: their a_1 parameters cover the range 0.68–2.57. The overall average value of a_1 for low-redshift FRI sources is 1.39 ± 0.094 indicating that at $z < 0.5$ FRI sources, as expected, generally prefer the relatively higher density environments. Of the 12 low-redshift FRIs, only three sources are in underdense environments and these have an average value of 0.86 for a_1 . Our sample includes only a small number of FRII sources at low redshifts (only four sources in all). We have omitted the source J0046.2–6637 for which the identification of the host galaxy is uncertain and the source J0044.3–6746 that has a bright star nearby, leaving four FRII sources at low redshifts. Three of the four of these low- z FRIIs are found to have relatively rich environs, with average value of 1.33 ± 0.159 for a_1 . We note that the environmental richness parameter a_1 is similar for the low-redshift FRIs compared to the low-redshift FRIIs in our ATLBS samples. The above comparison between FRI/FRII sources at high and low redshift is depicted graphically in Fig. 6.

An examination of the FRI subsample as a whole reveals that the FRI sources inhabit environments that are more or less similar, over the redshift range examined here, barring the extreme outliers. And a similar result appears to emerge for FRIIs as well: their subsamples formed above and below redshift of 0.5 display similar a_1 coefficients on the average, see Figs 5(b) and 6. The weighted mean values of a_1 parameter for the selected 16 FRIs and nine FRIIs (Fig. 5b) are 1.38 ± 0.08 and 1.32 ± 0.12 . It may be noted here that we have separated the HT and WAT sources from this comparison: most HT and WAT sources are FRII and these clearly lie in more overdense regions compared to our FRI sample (which has HT and WAT sources excluded). Our study suggests that the FRIs and FRIIs may have similar environments and occur in moderately overdense

galaxy distribution space within galaxy groups and filaments of the large-scale structure; however, the WAT and HT sources inhabit the more extreme overdensities of clusters of galaxies. As is expected in structure formation, the highest density regimes that include clusters of galaxies evolve most rapidly at low redshifts and, therefore, it is unsurprising that redshift evolution across a $z = 0.5$ boundary appears to be significant only for the WAT sources.

7.3 Dipole and quadrupole environmental anisotropy

Next, we examine the environmental parameters a_2 – a_5 . These provide information regarding the dipole and quadrupole *angular* distribution of the overdensity in the vicinity of the sample sources. If the distribution of the overdensity about the radio source is uniform, then these parameters would be expected to vanish. If the distribution is non-uniform, then the parameters may have non-zero values and the sign of each parameter gives further information regarding the angular distribution. In practice, the value of the parameter is compared with the standard deviation for that parameter to estimate the significance. The arguments of the weighting functions f_k are the angles of the points in the grid with respect to the radio axis.

a_2 and a_3 measure the dipole anisotropy in density distribution. The parameter a_2 , which is the overdensity weighted with a sine function, is a measure of the side-to-side density difference on the two sides of the radio axis. The sign of a_2 indicates which side of the source is overdense, and there is no reason to expect any preference for the sign. The parameter a_2 would be expected to average to zero for any population of sources because the sign of this parameter would be equally likely to be positive and negative, although individual sources may have a significant magnitude. The parameter a_3 is the integral of the azimuthal variation in overdensity weighted with a cosine function. This parameter is of importance when examining asymmetric sources because it is a measure of the overdensity along the radio axis. A positive sign implies that the density in the direction of the longer radio lobe is higher than that towards the shorter radio lobe, and a negative sign implies the opposite.

a_4 and a_5 measure the quadrupole anisotropy in galaxy density distribution about the radio source. The parameter a_4 is the integral overdensity weighted with a sine function for which the argument is twice the PA with respect to the source axis. This parameter is a matched filter for a quadrupole angular anisotropy in overdensity that has maxima or minima at angles of $\pi/4$ and $5\pi/4$ to the radio axis. A positive sign for this parameter implies that the quadrupole anisotropy has overdensities at angles of $\pi/4$ and $5\pi/4$ from the direction defined by the vector towards the more extended lobe, and a negative sign implies that the overdensity is along $3\pi/4$ and $7\pi/4$. The last parameter a_5 is weighted by a cosine function that once again has argument twice the PA with respect to the source axis. This parameter is sensitive to quadrupole anisotropy in density that has maxima along the radio axis or along a direction perpendicular to the source axis. A positive sign for this parameter implies that the overdensity along the radio axis is larger than off the axis, and a negative sign implies that the overdensity in a direction perpendicular to the radio axis is larger. Together, these parameters a_2 – a_5 provide a good description of the dipole and quadrupole distribution of the density in the environments of radio sources.

The parameter a_3 , which is a measure of the environmental dipole overdensity along the radio axis, has a value consistent with zero (within errors) for most of the source types except HT sources. The weighted mean a_3 is 0.123 ± 0.046 (for HT sources), 0.018 ± 0.02

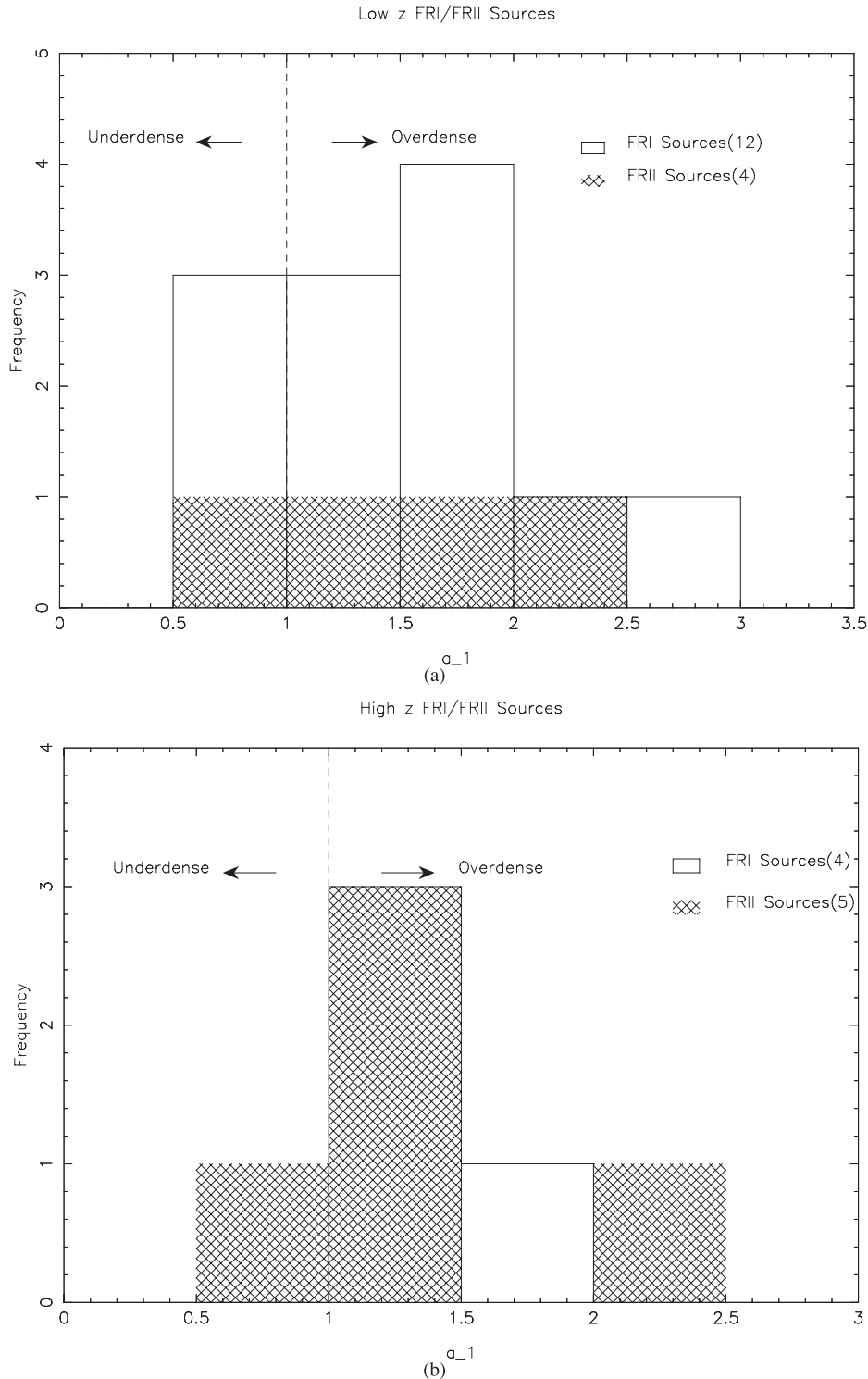


Figure 6. Comparative view of the overdensity (as characterized by the parameter a_1) of (a) low-redshift FRI versus FRII sources and (b) high-redshift FRI and FRII sources.

(for FRI source subsample), -0.021 ± 0.027 (for FRII sources) and -0.044 ± 0.037 (for WAT sources). The weighted mean value of a_3 is significant only for the HT population and it is notable that the value of a_3 for all of the HT sources is positive. These suggest that the tail of head-tail sources preferentially – and in all cases in our ATLAS-ESS subsample of HT sources – points in the direction of higher local galaxy density. This result may be interpreted in sev-

eral ways. One explanation may be that the host galaxies of these HT sources are orbiting around the cluster centre and currently in projection the hosts are moving away from the cluster centres with the tails pointing back towards the cluster centre. Alternatively, the sources may be in clusters undergoing merger events and the tails of the HT sources are being dragged by the intracluster weather towards the cluster centre.

Table 3. The asymmetric source subsample along with the parameters a_k and the standard deviations in each of the parameters. Various columns follow the same scheme as that for Table 1.

Source name	Extended source name	Redshift	Source type	PA	a_1	σ_{a_1}	a_2	σ_{a_2}	a_3	σ_{a_3}	a_4	σ_{a_4}	a_5	σ_{a_5}
J0024.4–6636	J002426–663612	0.21	I	90	$2.57^{2.57}_{2.57}$	0.4	$0.09^{0.1}_{0.07}$	0.1	$-0.15^{-0.14}_{-0.16}$	0.11	$0.03^{0.02}_{0.04}$	0.04	$0.04^{0.04}_{0.03}$	0.04
J0045.5–6726	J004532–672635**	0.27	I	72	$1.93^{1.93}_{1.93}$	0.46	$0.01^{0.21}_{0.03}$	0.1	$0.21^{0.21}_{0.21}$	0.09	$0.01^{0.01}_{0.03}$	0.03	$0.13^{0.13}_{0.13}$	0.03
J0057.2–6651	J005707–665059	0.24*	I	112	$1.82^{1.82}_{1.82}$	0.41	$0.1^{0.1}_{0.09}$	0.08	$-0.03^{-0.02}_{-0.03}$	0.08	$-0.03^{-0.04}_{0.03}$	0.03	$0.04^{0.04}_{0.05}$	0.03
J0101.1–6600	J010107–660018	0.24	II	174	$0.81^{0.81}_{0.81}$	0.3	$0.02^{0.02}_{0.02}$	0.07	$-0.01^{-0.01}_{-0.02}$	0.08	$0.03^{0.02}_{0.03}$	0.03	$0.04^{0.04}_{0.03}$	0.03
J0102.6–6658	J010238–665813**	0.61	I	40	$1.46^{1.46}_{1.46}$	0.4	$0.07^{0.09}_{0.05}$	0.11	$-0.24^{-0.23}_{-0.25}$	0.11	$-0.02^{-0.03}_{0.05}$	0.05	$0.04^{0.03}_{0.04}$	0.04
J0103.2–6614	J010315–661425	0.33*	II	186	$1.17^{1.17}_{1.17}$	0.28	$0.02^{0.02}_{0.02}$	0.08	$-0.04^{-0.04}_{-0.05}$	0.08	$0^0_{0.03}$	0.03	$0.01^{0.01}_{0.01}$	0.03
J0103.7–6632	J010344–663227	0.59	II	–90	$1.2^{1.2}_{1.2}$	0.37	$0.04^{0.05}_{0.03}$	0.11	$-0.12^{-0.11}_{-0.12}$	0.1	$0.02^{0.01}_{0.04}$	0.04	$0.04^{0.05}_{0.04}$	0.05

7.4 Asymmetric ATLBS-ESS sources

We next examine the sources which exhibit significantly asymmetric radio morphology. A subsample of ‘asymmetric’ sources was compiled on the basis of lobe asymmetry; for inclusion in this subsample, one of the lobes is required to be more than 1.5 times the extent of the opposite lobe. With this selection criterion, we find seven asymmetric sources in ATLBS-ESS. We have presented the asymmetric source sample separately in Table 3.

We have examined the environmental parameters for the selected asymmetric sources. Almost all the asymmetric sources in our sample appear to lie in rich environments, as indicated by high to moderate values of a_1 ; the one exception is J0101.1–6600, which has an a_1 parameter corresponding to an underdense region. We note that all the asymmetric sources, except J0045.5–6726, show negative values for the parameter a_3 , which is a clear indication that the ambient galaxy density is almost always higher in the direction of the shorter lobe. The weighted mean value for a_3 is -0.0359 ± 0.0341 . The latter value is significant when taken in the context of the values of a_3 for the subsample of *symmetric* sources. The values of a_3 parameter are positive or negative for symmetric sources, without any significant preference towards positive or negative sign. In comparison, all except one of the sources in the asymmetric source sample have a negative sign for the value of the a_3 parameter. Examined in this light, the distribution of the a_3 parameter is significant.

All of the asymmetric sources have a positive a_5 and the weighted mean a_5 for the asymmetric sources is significantly 0.051 ± 0.013 . This implies that asymmetric radio sources are usually aligned along the line of excess galaxy density with a quadrupole asymmetry apart from any dipole component. It may be that when double radio sources are created by jets that happen to be aligned with galaxy overdensity, and the galaxy clustering is on one side, the associated gas inhibits jet advance via ram pressure interaction and it is radio galaxies in such environmental circumstances that display grossly asymmetric morphology. It may also be noted that none of the subsamples of sources, except the asymmetric sources, shows significant values of a_5 . In most of the asymmetric cases, there is more galaxy overdensity on the shorter side, consistent with the expectations that gas density follows galaxy density and the side with higher gas density would be expected to be shorter owing to slower advance speed for the jets. The positive value of a_5 , together with a negative value of a_3 for most of the sample implies that the environmental overdensity is not a gradient but is a concentration in the direction of the shorter lobe. The a_4 parameter for these asymmetric sources has less significance in magnitude and appears random in signs, as expected. Curiously, the parameter a_2 for this

sample is positive for all of the asymmetric sources; however, the weighted mean a_2 is 0.048 ± 0.034 and is not significant.

All of the six asymmetric sources with negative values for a_3 have linear size in the range 400–600 kpc. J0045.5–6726, which alone has a positive value for a_3 , has a significantly smaller linear size of 164 kpc and, therefore, the anomalous behaviour for this source may be understood as arising from its relatively small size due to which the lobe extent may be more influenced by the local interstellar medium of the host galaxy rather than the intergalactic gas associated with the large-scale galaxy distribution, which is what is probed by our approach. The high value of a_1 for the FRI source J0045.5–6726 indicates a rich environment for this source; however, the positive sign for a_3 implies that the longer side of the source is in denser regions. Additionally, the source has a high value for a_5 , showing that the density distribution is along the radio axis. This source has an FRI morphology and an alternate explanation for the positive value of a_3 for this source may be that the higher galaxy density on the longer side preserves the diffuse emission on that side by limiting expansion losses.

8 SUMMARY

We have presented details of optical observations and data reduction for the ATLBS regions. The optical observations were used to determine the redshifts and magnitudes of the ATLBS-ESS sample of radio sources formed of the extended radio sources detected in the ATLBS. In this study, galaxy catalogues constructed from the optical data were utilized to estimate the environmental parameters of selected sources from the ATLBS-ESS sample. We have defined a set of parameters a_1 – a_5 to quantify the local galaxy overdensity and its angular anisotropy with respect to the axis of the radio sources using smoothed galaxy density maps. Dipole and quadrupole anisotropy has been estimated for the individual sources and these measures have been stacked (averaged) to estimate mean measures and their errors for different classes of radio source morphologies.

Examining the anisotropy parameters for a subsample of extended double radio sources that includes all sources with pronounced asymmetry in lobe extents, we find good evidence for environmental anisotropy being the dominant cause for lobe asymmetry in that higher galaxy density occurs almost always on the side of the shorter lobe, and this validates the usefulness of the method proposed and adopted here. The environmental parameters have been used to examine and compare the environments of FRI and FRII radio sources in two redshift regimes ($z < 0.5$ and $z > 0.5$). WAT sources and HT sources lie in the most overdense environments. The head–tail source environments display dipolar

anisotropy in that higher galaxy density appears to lie in the direction of the tails. Excluding the head–tail and wide-angle tail sources, subsamples of FRI and FRII sources from the ATLBS appear to lie in similar moderately overdense environments, with no evidence for redshift evolution in the regimes studied herein.

ACKNOWLEDGEMENTS

KT and LS would like to thank Dr Helen Johnston for providing the spectroscopic data. We also thank the referee for helpful comments on the earlier draft of this paper.

IRAF is distributed by the National Optical Astronomy Observatories, which are operated by the Association of Universities for Research in Astronomy, Inc., under cooperative agreement with the National Science Foundation.

REFERENCES

- Abell G. O., 1958, *ApJS*, 3, 211
 Alvarado F., Wenderoth E., Alcaïno G., Liller W., 1995, *AJ*, 110, 646
 Bertin E., Arnouts S., 1996, *A&AS*, 117, 393
 Best P. N., Lehnert M. D., Miley G. K., Rottgering H. J. A., 2003, *MNRAS*, 343, 1
 Blanton E. L., Randall S. W., Clarke T. E., Sarazin C. L., McNamara B. R., Douglass E. M., McDonald M., 2011, *ApJ*, 737, 99
 Boehringer H., Voges W., Fabian A. C., Edge A. C., Neumann D. M., 1993, *MNRAS*, 254, 25
 Burns J. O., Loken C., Roettiger K., Rizza E., Bryan G., Norman M. L., Gómez P., Owen F. N., 2002, *New Astron. Rev.*, 46, 135
 Chen R., Peng B., Strom R. G., Wei J., 2012, *MNRAS*, 420, 2715
 Chilingarian I. V., Melchior A., Zolotukhin I., 2010, *MNRAS*, 405, 1409
 Eales S., Rawlings S., Duncan L., Cotter G., Lacy M., 1997, *MNRAS*, 291, 593
 Fanaroff B. L., Riley J. M., 1974, *MNRAS*, 167, 31
 Fukugita M., Shimasaku K., Ichikawa T., 1995, *PASP*, 107, 945
 Gal R., 2008, in Plionis M., López-Cruz O., Hughes D., eds, *Lecture Notes in Physics*, Vol. 740, *A Pan-Chromatic View of Clusters of Galaxies and the Large-Scale Structure*. Springer, Dordrecht, p. 119
 Gendre M. A., Best P. N., Wall J. V., 2010, *MNRAS*, 404, 1719
 Hardcastle M. J., 2004, *A&A*, 414, 927
 Hatch N. A. et al., 2011, *MNRAS*, 410, 1573
 Hill G., Lilly S., 1991, *ApJ*, 367, 1
 Kim R. et al., 2002, *AJ*, 123, 20
 Longair M. S., Seldner M., 1979, *MNRAS*, 189, 433
 McCarthy P. J., van Breugel W., Kapahi V. K., 1991, *ApJ*, 371, 478
 Mauch T., Murphy T., Buttery H. J., Curran J., Hunstead R. W., Pietrzynski B., Robertson J. G., Sadler E. M., 2003, *MNRAS*, 342, 1117
 Metcalfe N., Shanks T., Fong R., Jones L. R., 1991, *MNRAS*, 249, 498
 Overzier R. A. et al., 2008, *ApJ*, 673, 143
 Owen F. N., Rudnick L., 1976, *ApJ*, 205, L1
 Popesso P., Böhringer H., Romaniello M., Voges W., 2005, *A&A*, 433, 415
 Postman M., Lubin L. M., Gunn J. E., Oke J. B., Hoessel J. G., Schneider D. P., Christensen J. A., 1996, *AJ*, 111, 615 (P96)
 Safouris V., Subrahmanyan R., Bicknell G. V., Saripalli L., 2009, *MNRAS*, 393, 2
 Saripalli L., Subrahmanyan R., Thorat K., Ekers R. D., Hunstead R. W., Johnston H. M., Sadler E. M., 2012, *ApJS*, 199, 27
 Subrahmanyan R., Saripalli L., Safouris V., Hunstead R. W., 2008, *ApJ*, 677, 63
 Subrahmanyan R., Ekers R. D., Saripalli L., Sadler E. M., 2010, *MNRAS*, 402, 2792
 Thorat K., Subrahmanyan R., Saripalli L., Ekers R. D., 2013, *ApJ*, 762, 16
 Varela J., D’Onofrio M., Fasano G., 2009, *A&A*, 497, 2009
 Wing J., Blanton E., 2011, *AJ*, 141, 88
 Yasuda N. et al., 2001, *AJ*, 122, 1104
 Yee H. K. C., Green R. F., 1984, *ApJ*, 280, 79
 Zhao Y., Huang J., Ashby M., Fazio G., Miyazaki S., 2009, *Res. Astron. Astrophys.*, 9, 1061
 Zirbel E., 1997, *ApJ*, 476, 489

This paper has been typeset from a $\text{\TeX}/\text{\LaTeX}$ file prepared by the author.